

CHEMICAL KINETICS  
AND CATALYSIS

## Selective Oxidation of Glycerol to Lactic Acid over Supported Bimetallic Au–M Catalysts

Yi-Hu Ke<sup>a,b,c,\*</sup>, Xue Wang<sup>a,b,c</sup>, Jing-Yun Li<sup>a,b,c</sup>, Hai Liu<sup>a,b,c</sup>, and Hong Yuan<sup>a,b,c</sup>

<sup>a</sup> School of Chemistry and Chemical Engineering, North Minzu University, Yinchuan, 750021 China

<sup>b</sup> Key Laboratory of Chemical Engineering and Technology, State Ethnic Affairs Commission, North Minzu University, Yinchuan, 750021 China

<sup>c</sup> Ningxia Key Laboratory of Solar Chemical Conversion Technology, North Minzu University, Yinchuan, 750021 China

\* e-mail: keyihu123@nmu.edu.cn

Received October 8, 2020; revised October 8, 2020; accepted December 11, 2020

**Abstract**—A series of bimetallic Au–M (Pt, Pd, Cu, Ir, Ag) catalysts supported on composite oxide were prepared through the deposition of pre-formed Au–M colloids. These catalysts were evaluated in the selective oxidation of glycerol to lactic acid. The results showed that MgLaO composite oxide supported Au–Pt catalyst has the optimal catalytic activity and selectivity. Furthermore, it was found that the category of the second active component has great influence on the catalytic activity of Au–M/MgLaO (M = Pt, Pd, Cu, Ir, Ag) catalysts. XRD, XPS, TEM, HRTEM, and H<sub>2</sub>-TPR analyses demonstrated that the structure of the supports and the interaction between Au and the second active component had an effect on catalytic activity and selectivity. Meanwhile, the Au–Pt/MgLaO catalyst also presented great performance in recyclability without any obvious change in catalytic activity, but a little decrease of selectivity was observed after 7 cycles.

**Keywords:** glycerol, catalytic oxidation, lactic acid, composite oxides, bimetallic supported catalysts

10.1134/S0036024421150139

### INTRODUCTION

With the depletion of non-renewable resources, the development and utilization of renewable resources had been attracting more and more attention in academia and industry. As a renewable energy source, the production of biodiesel had increased year by year [1, 2]. However, a large amount of by-product glycerol produced during the production of biodiesel, which not only causes a sharp drop in price of glycerin, but also a severe restriction on the development of biodiesel industry. Therefore, the effective use of redundant glycerol is an important way to improve the economics of the biodiesel process. And one important utilization method is the conversion of glycerol to lactic acid.

As a multi-functional platform compound, lactic acid is a fine chemical which can be widely used in food, medicine, tanning, textile, environment, and agriculture [3–5]. Many down-stream products with high application value can also be obtained from lactic acid as raw material via different reactions [6–8]. At present, there are three main methods to produce lactic acid by liquid phase conversion of glycerol: hydrolysis [9–12], hydrogenolysis [13, 14], and oxidation [15–18]. Among them, catalytic oxidation technology had always been concerned because of mild reaction condition.

The supported bimetallic catalyst showed good catalytic performance in the liquid-phase catalytic oxidation of glycerol to lactic acid. In 2010, Shen et al. [19] synthesized lactic acid using Au–Pt/TiO<sub>2</sub> catalysts for the first time, achieving the selectivity towards lactic acid of 85.6%. Liu et al. [20] and Heeres et al. [21, 22], respectively used Au–Pd/TiO<sub>2</sub>, Au–Pt/nCeO<sub>2</sub> and Au–Pt/USY-600 as catalysts to catalyze the oxidation of glycerol to lactic acid under different conditions. Zhang et al. [23] prepared Pt–Cu/AC catalyst by modifying Pt with Cu. Li et al. [24] prepared Pt<sub>1</sub>Ni<sub>1</sub>O<sub>x</sub>/TiO<sub>2</sub> catalyst by modifying Pt with Ni, and Cho et al. [25] prepared Pt/Sn-MFI catalyst by supporting Pt on Sn-modified MFI. These catalysts were used in the oxidation of glycerol to lactic acid with high selectivity under mild conditions.

However, the supported bimetallic catalysts with a fixed ratio of metallic components are usually evaluated. What's more, there is no systematic and comparative study on the catalysis of the second active component and which of them is the best. In this work, the catalytic performance of Au–Pt catalysts supported on composite oxides such as Mg–Al, Mg–Ce, and Mg–La was compared during the catalytic oxidation of glycerol to lactic acid. The effects of different second active components, like Pt, Pd, Cu, Ir, and Ag were also investigated.

## 1. EXPERIMENTAL SECTION

### 1.1. Catalyst Preparation

MgMO (M = Al, La, Ce) composite oxides were prepared by a deposition-precipitation method. Preparation of MgAlO composite oxide is described as an example. Typically,  $\text{Mg}(\text{NO}_3)_2 \cdot 6\text{H}_2\text{O}$  (0.03 mol),  $\text{Al}(\text{NO}_3)_3 \cdot 9\text{H}_2\text{O}$  (0.024 mol), and urea (0.54 mol) were added to deionized water (300 mL) under stirring at room temperature, and then the pH was adjusted to  $\sim 2.0$  with  $\text{HNO}_3$ . The resulting mixture was continuously stirred for 24 h at  $90^\circ\text{C}$ . The solid was separated by filtration and washed repeatedly with deionized water to neutral. The resultant solid was dried at  $100^\circ\text{C}$  for 16 h and calcined at  $900^\circ\text{C}$  for 1 h under still air. The same procedure was used to prepare MgLaO and MgCeO composite oxides.

The supported catalysts were prepared by colloidal deposition method. The preparation of supported Au catalyst is described as an example. Typically,  $\text{HAuCl}_4$  solution (0.0283 M), PVA (metal M/PVA =  $2 \text{ mg mg}^{-1}$ ) were added to deionized water (50 mL) under stirring at room temperature for 30 min. Subsequently, freshly prepared  $\text{NaBH}_4$  solution (0.1 M,  $\text{Au}/\text{NaBH}_4 = 1 : 4 \text{ mol mol}^{-1}$ ) was added rapidly and the mixture was stirred for another 30 min, which led to the formation of colloids. Then, the support (1 g) was dispersed in the obtained dispersion with continuous stirring for 4 h. The solid sample was collected by filtration and washed with deionized water until no  $\text{Cl}^-$  can be detected in the wash water. Finally, the obtained precipitate was dried at  $60^\circ\text{C}$  for 12 h under vacuum. The same procedure was used to prepare the bimetallic supported catalysts. Two different metal precursor solutions were added in a certain metal ratio, the other conditions are the same as in the method for preparing a single metal catalyst.

### 1.2. Catalysts Characterization

The specific surface areas and the pore structure of the catalysts were determined using a Micromeritics ASAP2020M system. X-ray diffraction (XRD) patterns of the catalysts were obtained on Rigaku Smart Lab X-ray diffractometer with a  $\text{CuK}_\alpha$  radiation source. Transmission electron microscopy (TEM) images were obtained using FEI-Tecnaï G2 F20 instrument. The particle size distribution and lattice spacing of metal nanoparticles were determined from TEM images. Reduction of the catalyst precursors was studied by  $\text{H}_2$  temperature-programmed reduction ( $\text{H}_2$ -TPR) using a Micromeritics AutoChem II-2920 instrument. The elemental contents were determined by inductively coupled plasma optical emission spectroscopy (ICP-OES, Prodigy7, Teledyne Leeman Labs). X-ray photoelectron spectroscopy (XPS) analyses were performed using an AXIS ULTRA spectrometer with an  $\text{AlK}_\alpha$  radiation source (1486.6 eV).

### 1.3. Catalytic Performance

The liquid-phase glycerol oxidation was carried out in a 35 mL stainless steel autoclave equipped with a mechanical stirring and a temperature control system. Firstly, the catalyst, NaOH, and 0.17 M glycerol aqueous solution (24 mL) were added into the autoclave. When oxygen was fed into the reactor to desired pressure of 5 bar at room temperature, the temperature of the reactor was heated to  $100^\circ\text{C}$  in 20 min. After 4 h of reaction, the autoclave was cooled to room temperature with an ice-water bath. Then, the sample was centrifuged and analyzed by high-performance liquid chromatography (HPLC) using an Aminex HPX-87H column with UV (210 nm) and refractive index (RI) detector. The mobile phase was diluted with 0.005 M  $\text{H}_2\text{SO}_4$  solution (flow 0.5 mL/min).

## 2. RESULTS AND DISCUSSION

### 2.1. Catalyst Characterization

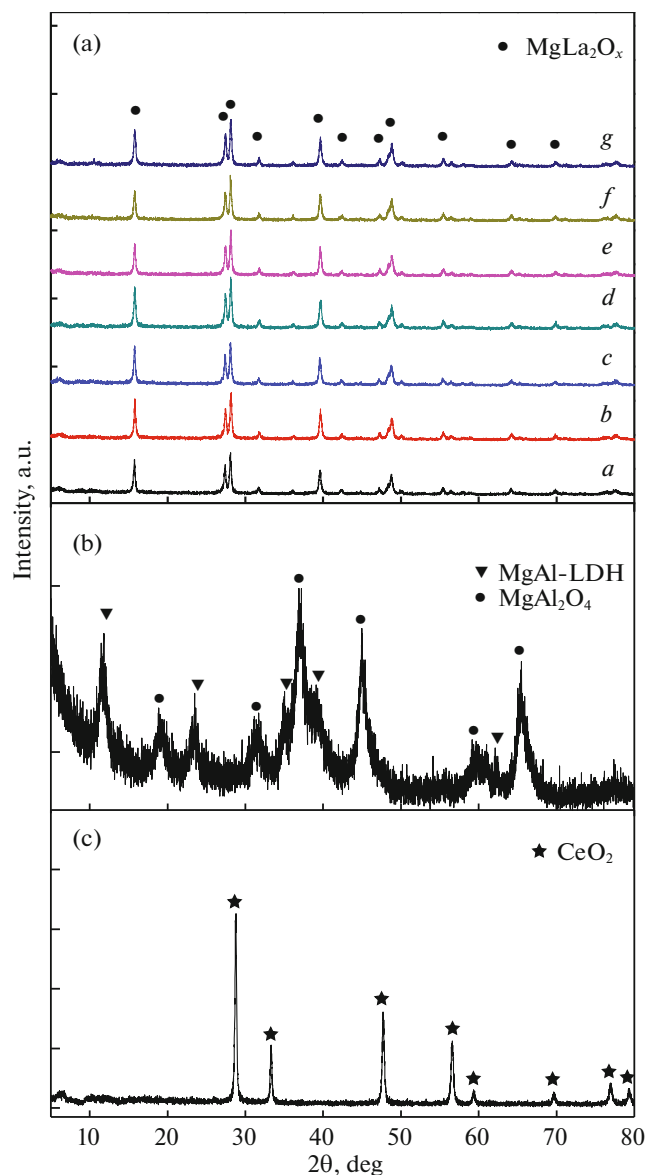
The textural properties and elements content of the catalysts are presented in Table 1. The Au–Pt/MgAlO catalyst shows the largest specific surface areas (i.e.,  $117.1 \text{ m}^2 \text{ g}^{-1}$ ) and pore volume ( $0.41 \text{ m}^3 \text{ g}^{-1}$ ). The Au–Pt/MgCeO catalyst has the lowest specific surface areas ( $8.9 \text{ m}^2 \text{ g}^{-1}$ ) and pore volume ( $0.03 \text{ m}^3 \text{ g}^{-1}$ ). The catalysts supported on MgLaO show medium specific surface areas ( $14.2\text{--}24.1 \text{ m}^2 \text{ g}^{-1}$ ) and pore volume ( $0.06\text{--}0.08 \text{ m}^3 \text{ g}^{-1}$ ). Differently, the average pore diameter of all catalysts was in the range of 13 to 17 nm.

The actual loading of Au and Pt in Au/MgLaO and Pt/MgLaO catalysts is 2.1 and 2.22 wt %, respectively, which is lower than the theoretical loading of 3 wt %. This may be related to the properties of support, or the interaction between active metal and support. Compared with the supported monometallic catalyst, the actual loading of the supported bimetallic catalysts is close to theoretical value. It is possible that the sol is easier to be deposited on the supports due to the interaction of Au and second active component M.

XRD patterns of various supported catalysts are shown in Fig. 1. The diffractograms of Au/MgLaO, Au–Pt/MgLaO, Au–Pd/MgLaO, Au–Cu/MgLaO, Au–Ir/MgLaO, Au–Ag/MgLaO, and Pt/MgLaO catalysts are presented in Fig. 1a. The catalysts have characteristic diffraction peaks at  $2\theta = 15.6^\circ, 27.2^\circ, 27.9^\circ, 31.6^\circ, 39.5^\circ, \text{ and } 48.7^\circ$ , corresponding to the crystalline phase of MgLaO (JCPDS 42-0339). Figure 1b shows the diffraction peaks of MgAl-LDH and  $\text{MgAl}_2\text{O}_4$ , which indicates that MgAl-LDH is not completely transformed into pure  $\text{MgAl}_2\text{O}_4$  spinel phase during the catalyst preparation. The diffraction peaks of  $\text{CeO}_2$  (JCPDS 01-0800) are shown in Fig. 1c. Moreover, no characteristic diffraction peaks of active contents were detected, which may be due to the high

**Table 1.** Active metal content and textural properties of various catalysts

Catalyst	Au loading, wt %	Pt/Pd/Cu/Ir/Ag Loading, wt %	Au/M, mol/mol	$S_{\text{BET}}$ , $\text{m}^2 \text{g}^{-1}$	$V_{\text{p}}$ , $\text{m}^3 \text{g}^{-1}$	$D_{\text{p}}$ , nm
Au/MgLaO	2.1	—	—	14.2	0.06	15.8
Au–Pt/MgAlO	2.6	0.68	3.81	117.1	0.41	14.2
Au–Pt/MgCeO	2.5	0.53	4.75	8.9	0.03	14.0
Au–Pt/MgLaO	2.4	0.60	3.88	15.9	0.07	16.5
Au–Pd/MgLaO	2.6	0.29	4.88	19.8	0.07	14.0
Au–Cu/MgLaO	2.7	0.50	0.35	20.0	0.07	14.0
Au–Ir/MgLaO	2.2	0.88	2.36	19.4	0.08	16.9
Au–Ag/MgLaO	2.2	0.59	2.01	20.6	0.07	14.4
Pt/MgLaO	—	2.22	—	24.1	0.08	13.4

**Fig. 1.** XRD patterns of various supported catalysts: (a) Au–M/MgLaO, (b) Au–Pt/MgAlO, (c) Au–Pt/MgCe.

dispersion and small particle size of active metals. This speculation is verified in the following TEM characterization.

TEM images of various catalysts and the corresponding particle size distribution of the supported metal particles are shown in Fig. 2. It is found that supported Au–Pt catalysts (Figs. 2b–2d) have similar particle size distribution. This shows that Au–Pt alloy was uniformly loaded on the support, which had a less effect by the support. After the reaction (Figs. 3b–3d), the particle size became larger, and the extent of the increase was basically the same. Figure 2a showed that Au/MgLaO catalyst has the largest Au particles and a wide distribution. After the reaction (Fig. 3a), the particle size of Au changed from  $5.9 \pm 1.7$  to  $7.1 \pm 1.7$  nm. On the contrary, as shown in Fig. 2i, the particle size of Pt/MgLaO catalyst has the smallest Pt particles and a narrow distribution, which reached  $1.39 \pm 0.2$  nm. The particle size basically remained unchanged after the reaction.

Compared to the monometallic Au/MgLaO and Pt/MgLaO catalysts, the Au–M/MgLaO catalysts (Figs. 2d–2h) have metal particles of moderate size and distribution, which were Au–Pt/MgLaO ( $2.1 \pm 0.4$  nm), Au–Pd/MgLaO ( $2.1 \pm 0.5$  nm), Au–Cu/MgLaO ( $2.5 \pm 0.4$  nm), Au–Ir/MgLaO ( $2.1 \pm 0.4$  nm), and Au–Ag/MgLaO ( $2.8 \pm 0.6$  nm), respectively. After the reaction (Figs. 3d–3h), the particle size of these catalysts increased variously except the Au–Ag/MgLaO. The Au–Pd/MgLaO catalyst has the most obvious increase, and the particle size increased from  $2.9 \pm 0.7$  to  $3.8 \pm 0.7$  nm. It can also be seen that except the Pt/MgLaO catalyst, the particles of others catalysts were uniformly dispersed and no agglomeration occurred during the reaction.

The morphology of the fresh catalyst was further characterized by HR-TEM to study the binding state between Au and M in supported Au–M catalysts, and the results are shown in Fig. 4. Figures 4a and 4i revealed that the lattice spacings were 0.237 and 0.224 nm, which corresponded to the characteristic

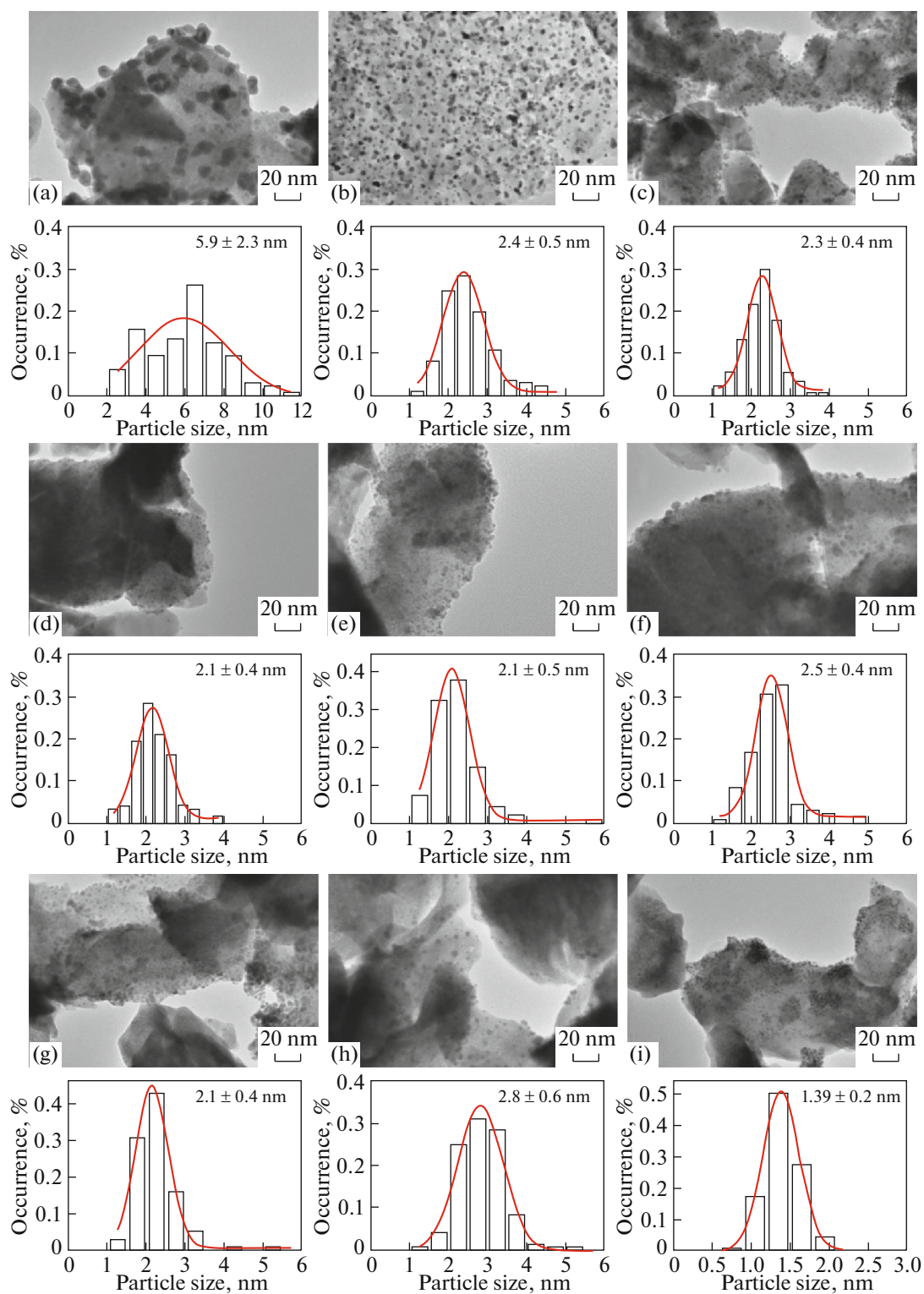


**Fig. 2.** TEM micrographs and the corresponding metal particle size distributions for fresh catalysts: (a) Au/MgLaO, (b) Au–Pt/MgAlO, (c) Au–Pt/MgCeO, (d) Au–Pt/MgLaO, (e) Au–Pd/MgLaO, (f) Au–Cu/MgLaO, (g) Au–Ir/MgLaO, (h) Au–Ag/MgLaO, (i) Pt/MgLaO.

Au (111) plane and Pt (111) plane, respectively [26, 27]. For the supported bimetallic Au–Pt catalysts (Figs. 4b–4d), the lattice spacing was between 0.230–

0.232 nm, which suggested that bimetallic Au–Pt alloy nanoparticles were successfully synthesized. The lattice space for other supported bimetallic Au–M cat-

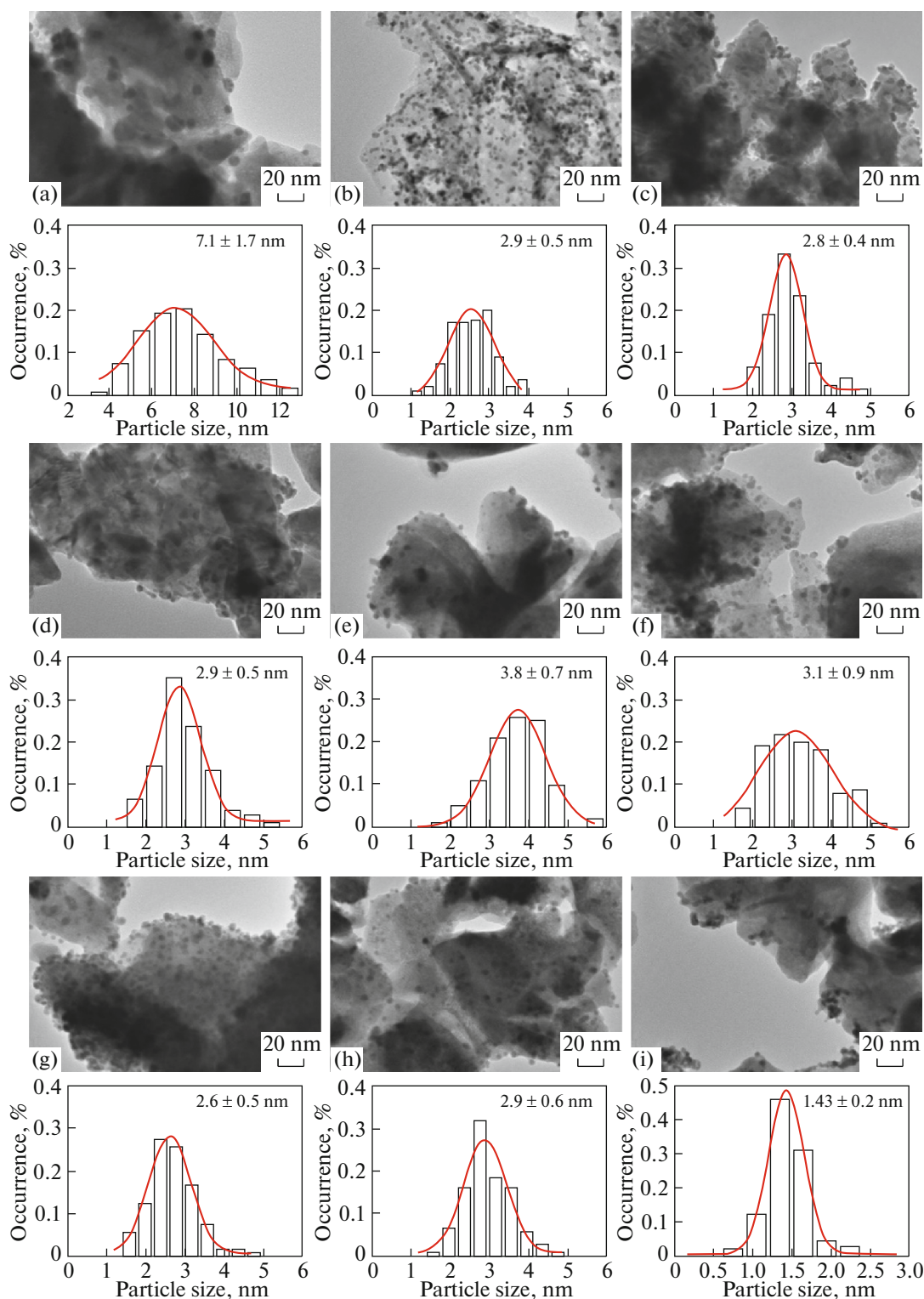


**Fig. 3.** TEM micrographs and the corresponding metal particle size distributions for used catalysts: (a) Au/MgLaO, (b) Au–Pt/MgAlO, (c) Au–Pt/MgCeO, (d) Au–Pt/MgLaO, (e) Au–Pd/MgLaO, (f) Au–Cu/MgLaO, (g) Au–Ir/MgLaO, (h) Au–Ag/MgLaO, (i) Pt/MgLaO.

alysts were 0.228 nm (Au–Pd), 0.223 nm (Au–Cu), 0.229 nm (Au–Ir), and 0.235 nm (Au–Ag), respectively, which were smaller than 0.237 nm of the

Au (111) plane and larger than the corresponding second metal (Figs. 4e–4h) [28–31]. This result suggested that the nanoparticles exist as bimetallic Au–M

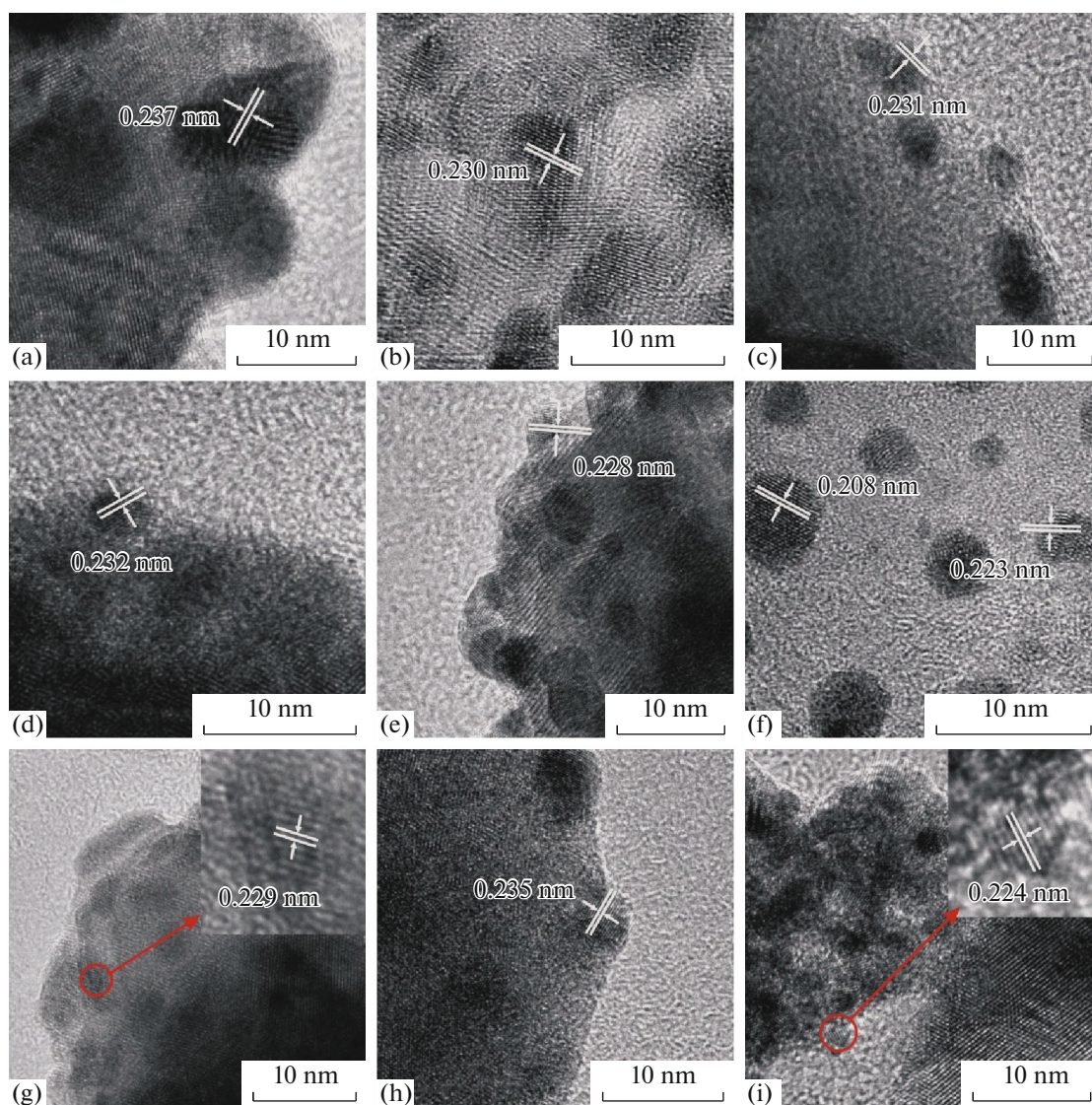


**Fig. 4.** HRTEM micrographs for the fresh catalysts: (a) Au/MgLaO, (b) Au-Pt/MgAlO, (c) Au-Pt/MgCeO, (d) Au-Pt/MgLaO, (e) Au-Pd/MgLaO, (f) Au-Cu/MgLaO, (g) Au-Ir/MgLaO, (h) Au-Ag/MgLaO, (i) Pt/MgLaO.

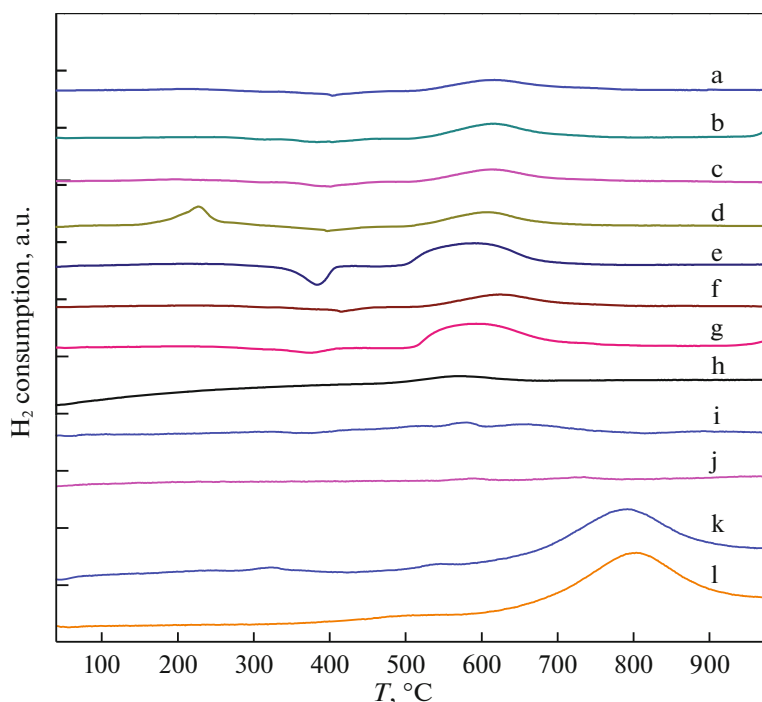
alloy. In addition, there were particles with the lattice spacing of 0.208 nm in the supported Au-Cu catalyst, which definitely means the presence of monometallic Cu in this catalyst.

Figure 5 shows  $H_2$ -TPR curves for all catalysts and corresponding supports. No  $H_2$  consumption peak was observed for MgLaO support (Fig. 5h), which suggests that MgLaO was not reduced in the studied temperature range. The lower  $H_2$  consumption peak for the Au-M/MgLaO catalysts around 600°C (Figs. 5a–5g) could be attributed to the reduction of lattice oxygen in the metal-support interface. In addition, the Au-Cu/MgLaO catalyst shows remarkable  $H_2$  consumption at 227°C, which could be ascribed to the reduction of  $Cu^+$  to metallic Cu. This observation agrees well with the previous studies [32, 33]. For the Au-

Ir/MgLaO catalyst, an unidentified inverted peak around 400°C was observed.

There was no  $H_2$  consumption observed for Au-Pt/MgAlO catalyst and MgAlO support (Figs. 5i and 5j), which suggests that all of them were not reduced in the studied temperature range. The Au-Pt/MgCeO catalyst and MgCeO support have a reduction peak around 800°C (Figs. 5k and 5l), which could be attributed to the reduction of bulk  $CeO_2$  [34, 35]. Furthermore, the reduction peak of the Au-Pt/MgCeO catalyst was lowered by 10°C compared to the MgCeO support, which may be due to the presence of a  $H_2$  spillover effect on the Au-Pt/MgCeO.

Electronic states and surface elemental composition of various catalysts were determined by XPS measurement, and the results are shown in Figs. 6, 7 and



**Fig. 5.** H<sub>2</sub>-TPR curves of various catalysts and MgLaO support: (a) Au/MgLaO, (b) Au–Pt/MgLaO, (c) Au–Pd/MgLaO, (d) Au–Cu/MgLaO, (e) Au–Ir/MgLaO, (f) Au–Ag/MgLaO, (g) Pt/MgLaO, (h) MgLaO, (i) Au–Pt/MgAlO, (j) MgAlO, (k) Au–Pt/MgCeO, (l) MgCeO.

Table 2. Except Au–Pt/MgCeO and Au–Cu/MgLaO catalysts, the Au 4f<sub>7/2</sub> binding energy in other catalysts is lower than that of bulk gold at 84.0 eV, which indicated that the Au clusters are in metallic state in these catalysts, as well as the presence of gold–support or gold–second active metal interactions. As for the Au–Cu/MgLaO catalysts, the Au 4f<sub>7/2</sub> binding energy was 84.1 eV, which indicated that the Au particles in this catalyst are in metallic state. The Au 4f<sub>7/2</sub> binding

energies were fitted by 83.6 and 85.6 eV for Au–Pt/MgCeO, which proved the presence of Au<sup>3+</sup> and Au<sup>0</sup> in this catalyst.

The XPS spectra of Pt 4f<sub>7/2</sub> are shown in Figs. 7a–7d. For Au–Pt/MgAlO, Au–Pt/MgLaO, and Pt/MgLaO catalysts, the binding energies of Pt 4f<sub>7/2</sub> are 71.0, 70.5, and 71.1 eV, respectively (Figs. 7a, 7c, 7d). These values are close to that of bulk platinum at

**Table 2.** Surface content and binding energies of the supported metals for various catalysts

Catalysts	Au <sub>surf</sub> (%)	M <sub>surf</sub> (%)	B.E. of Au 4f <sub>7/2</sub> (eV)	B.E. of M (eV)	BE of O 1s (eV)	Au/M atomic ratio
Au/MgLaO	0.57	—	83.5	—	531.0	—
Au–Pt/MgAlO	0.89	0.64	83.7	71	531.7	1.38
Au–Pt/MgCeO	0.99	0.21	83.6 (35.1%) 85.6 (64.9%)	72.7	532.7	4.67
Au–Pt/MgLaO	0.77	0.11	83.4	70.5	530.9	6.93
Au–Pd/MgLaO	0.64	0.16	83.3	334.6	531.2	2.16
Au–Cu/MgLaO	1.29	0.64	84.1	932.1(41.7%) 932.8(58.3%)	531.3	0.65
Au–Ir/MgLaO	0.90	0.14	83.6	61.7	530.8	6.27
Au–Ag/MgLaO	1.11	0.21	83.5	367.5	531.0	2.89
Pt/MgLaO	—	0.84	—	71.1	531.1	—

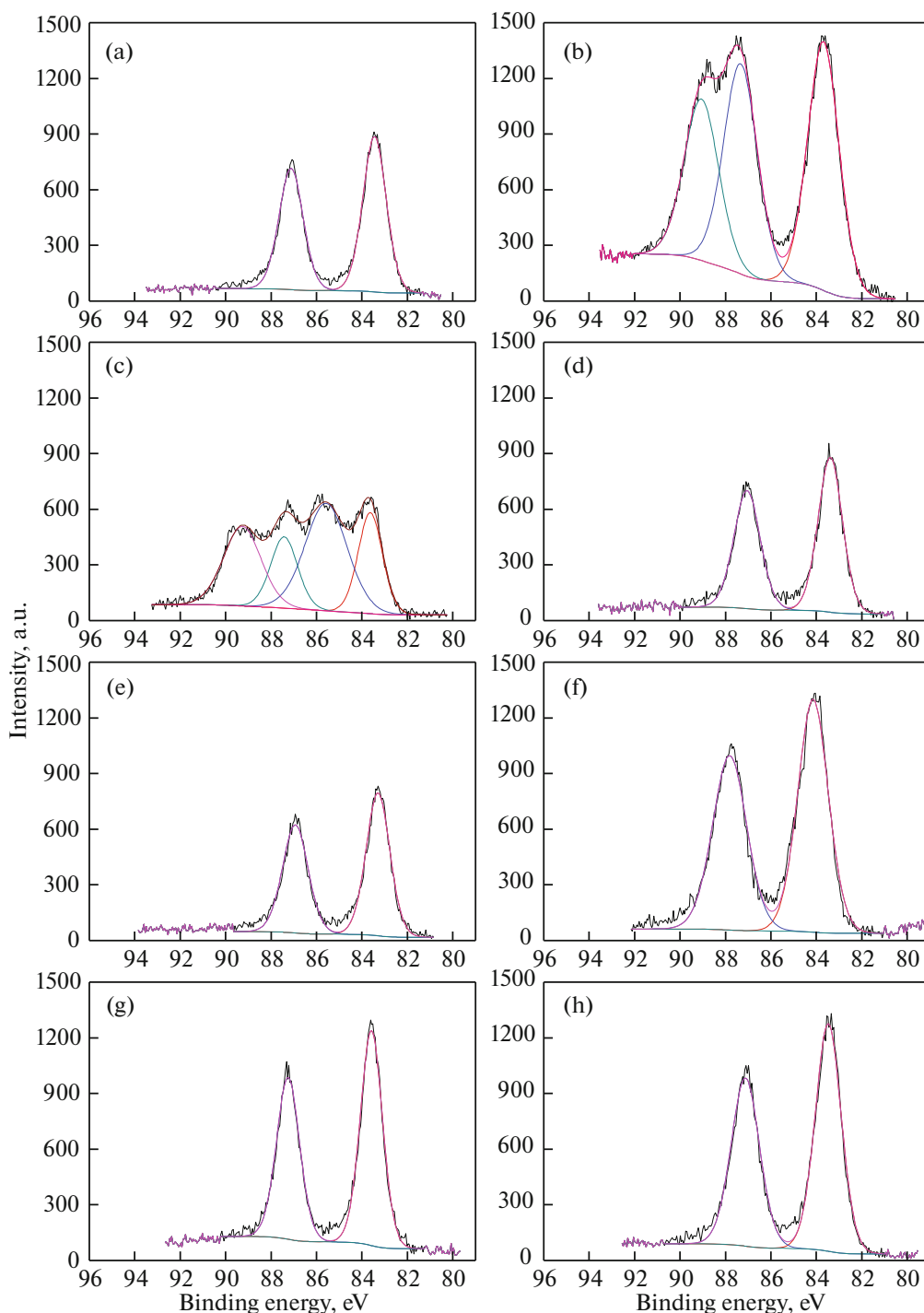


**Fig. 6.** Au 4f XPS spectra of various Au catalysts: (a) Au/MgLaO, (b) Au–Pt/MgAlO, (c) Au–Pt/MgCeO, (d) Au–Pt/MgLaO, (e) Au–Pd/MgLaO, (f) Au–Cu/MgLaO, (g) Au–Ir/MgLaO, and (h) Au–Ag/MgLaO.

71.2 eV [36–38], which indicates that the Pt clusters were in the metallic state. The binding energy of Pt  $4f_{7/2}$  is 72.7 eV for Au–Pt/MgCeO catalyst (Fig. 7c), which reveals the presence of  $Pt^{2+}$  [36].

The binding energy of Pd  $3d_{5/2}$  is 334.6 eV for Au–Pd/MgLaO catalyst (Fig. 7e). This value is slightly

smaller than that of bulk palladium at 335.3 eV, indicating that Pd is present in the catalyst as  $Pd^0$  [39, 40], and there is a certain interaction between Au–Pd. The binding energy of Ir  $4f_{7/2}$  is 61.7 eV for Au–Ir/MgLaO catalyst (Fig. 7f), indicating that Ir is present as  $Ir^{4+}$  [41], which may be due to the easy oxidation of Ir dis-



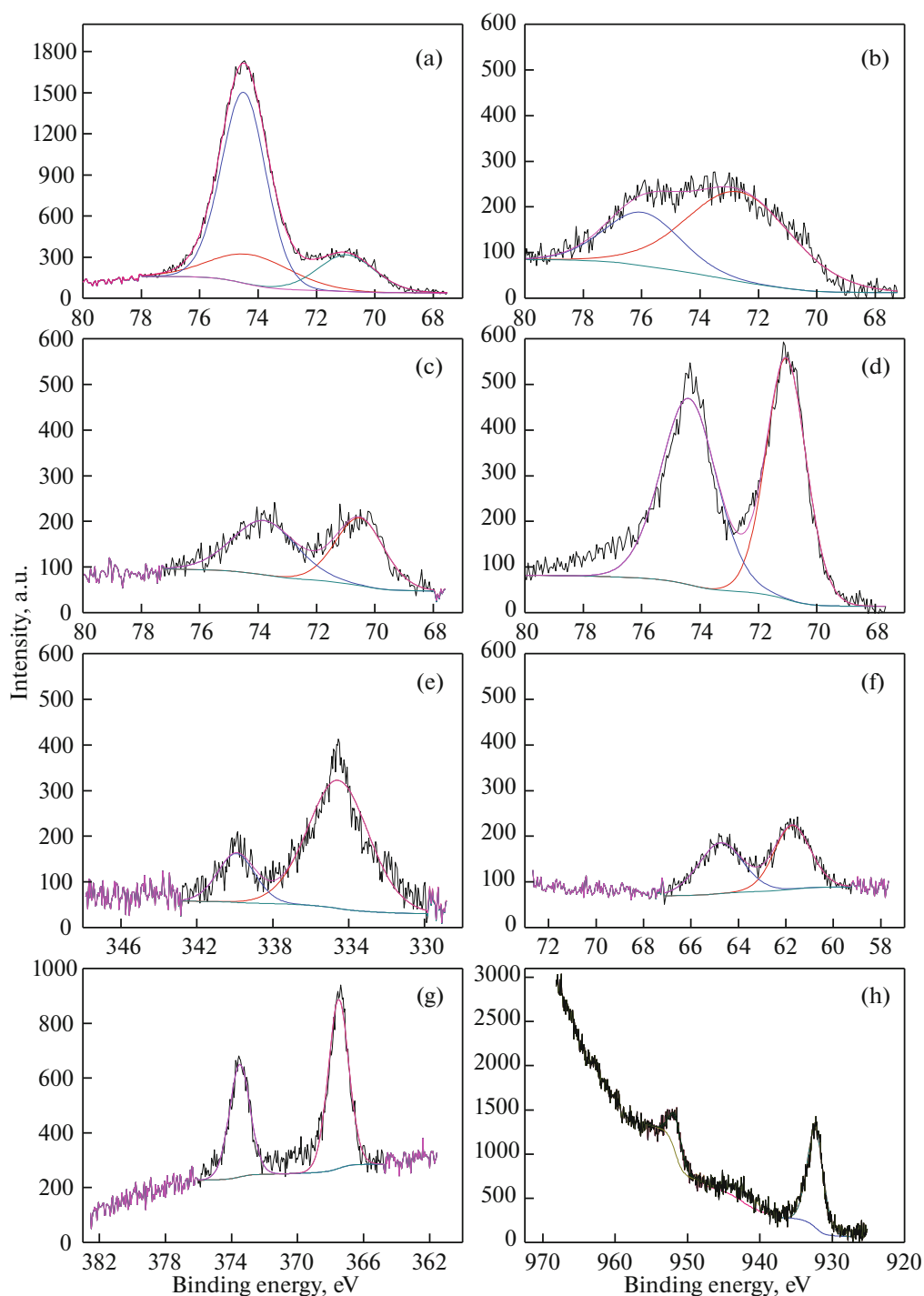


**Fig. 7.** XPS spectra of various catalysts: (a) Au–Pt/MgAlO, (b) Au–Pt/MgCeO, (c) Au–Pt/MgLaO, (d) Pt/MgLaO, (e) Au–Pd/MgLaO, (f) Au–Ir/MgLaO, (g) Au–Ag/MgLaO, and (h) Au–Cu/MgLaO.

persed on the surface of Au–Ir alloy. The binding energy of Ag  $3d_{5/2}$  is 367.5 eV for the Au–Ag/MgLaO catalyst (Fig. 7g), which is attributed to the presence of Ag<sup>2+</sup> in AgO [42]. In the Au–Cu/MgLaO catalyst, the binding energies of Cu  $2p_{3/2}$  were fitted to 932.1 and 932.8 eV (Fig. 7h). The binding energies correspond-

ing to the Cu  $2p_{3/2}$  of Cu, Cu<sub>2</sub>O, and CuO are 932.2, 932.6, and 933.2 eV, respectively [38]. So the first peak coincides with all phase states of elemental Cu, which is prone to oxidation in air. Therefore, Cu is present in the form of Cu<sup>0</sup> and Cu<sup>+</sup> in Au–Cu/MgLaO catalyst [43], which is consistent with the results of H<sub>2</sub>-TPR.

**Table 3.** Conversion of glycerol to lactic acid using supported monometallic and bimetallic catalysts

Catalyst	Conv., %	Selectivity, %					
		OA	TA	GLA	LA	FA	AA
Au/MgLaO	73.5	1.1	5.9	39.0	53.8	—	0.2
Au–Pt/MgAlO	87.6	1.4	3.9	27.1	63.4	—	4.2
Au–Pt/MgCeO	83.6	1.3	3.1	25.9	64.3	—	5.3
Au–Pt/MgLaO	83.1	1.2	2.4	20.2	70.9	—	5.2
Au–Pd/MgLaO	77.9	1.0	3.4	28.8	60.4	—	6.5
Au–Cu/MgLaO	63.0	3.9	3.1	48.4	35.4	6.4	2.8
Au–Ir/MgLaO	61.1	2.1	5.9	44.2	35.3	9.6	2.9
Au–Ag/MgLaO	54.6	3.5	7.6	36.3	36.5	11.2	4.9
Pt/MgLaO	80.7	1.6	2.1	16.8	76.7	—	2.9

Reaction conditions: glycerol (0.17 M, 24 mL), NaOH/GLY = 1 mol/mol, GLY/total metal intake = 680 mol/mol, 373 K, 4 h,  $P(O_2)$  = 5 bar. OA, oxalic acid, TA, tartaric acid, GLA, glyceric acid, LA, lactic acid, FA, formic acid, AA, acetic acid.

**Table 4.** Conversion of glycerol to lactic acid using supported bimetallic Au–Pt/MgLaO catalyst

Entry	Reaction time (h)	$P_{O_2}$ (bar)	NaOH/GLY (mol/mol)	GLY (M)	Conv. (%)	Selectivity, %					
						OA	TA	GLA	LA	FA	AA
1	2	5	1	0.17	69.0	0.6	1.3	18.8	69.5	4.8	5.0
2	4	5	1	0.17	83.1	1.2	2.4	20.2	70.9	—	5.2
3	6	5	1	0.17	86.2	1.3	2.0	22.6	67.7	—	6.4
4	4	3	1	0.17	70.0	0.6	1.1	16.3	77.3	—	4.7
5	4	10	1	0.17	86.0	2.1	2.9	26.7	61.1	—	7.3
6	4	5	4	0.17	92.9	0.6	2.2	18.8	76.3	0.4	1.7
7	4	5	1	0.1	83.9	2.2	3.2	29.9	57.9	—	6.9
8	4	5	1	0.3	68.6	0.4	0.7	13.5	77.9	4.9	2.6
9	4	5	1	0.45	45.0	0.4	0.7	16.9	79.2	1.0	1.8

Reaction conditions: glycerol (24 mL), glycerol/total metal intake = 680 mol/mol, 373 K.

## 2.2. Catalytic Performance

The results of performance evaluation of the supported bimetallic Au–M catalysts are shown in Table 3. In these experiments, the concentration of glycerol is 0.17 M, the molar ratio of glycerol to total metal content is 680 mol/mol, the molar ratio of NaOH to glycerol is 1 mol/mol, the initial partial pressure of oxygen is 5 bar, and the reaction is performed at 100°C for 4 h. As shown in Table 3, for the Au–Pt/MgAlO, Au–Pt/MgCeO, and Au–Pt/MgLaO catalysts, the catalytic activity differs insignificantly (the conversion values were 87.6, 83.6, and 83.1%, respectively), while the Au–Pt/MgLaO catalyst shows slightly higher selectivity for lactic acid. This result suggests that the support effect on catalytic performance was not significant in the selective oxidation of glycerol to lactic acid in alkaline conditions.

The bimetallic Au–M, monometallic Au and Pt catalysts supported on MgLaO composite oxide were taken as the primary catalysts to study the effect of the second active component on the catalytic oxidation of glycerol to lactic acid. The catalytic results were listed in Table 3. The glycerol conversion on Au/MgLaO and Pt/MgLaO was 73.5 and 80.7% with the corresponding lactic acid selectivity of 53.8 and 76.7%, respectively. Among the supported bimetallic Au–M catalysts, Au–Pt/MgLaO showed the best catalytic activity (glycerol conversion of 83.1% and lactic acid selectivity of 70.9%), followed by Au–Pd/MgLaO > Au–Cu/MgLaO > Au–Ir/MgLaO > Au–Ag/MgLaO. For the Au–Cu/MgLaO and Au–Ir/MgLaO catalysts, the main product was glyceric acid. For the Au–Ag/MgLaO catalyst, the selectivities towards glyceric acid and lactic acid were basically the same. The above results showed that the synergistic effect of Au–M played a key role in the catalytic oxi-

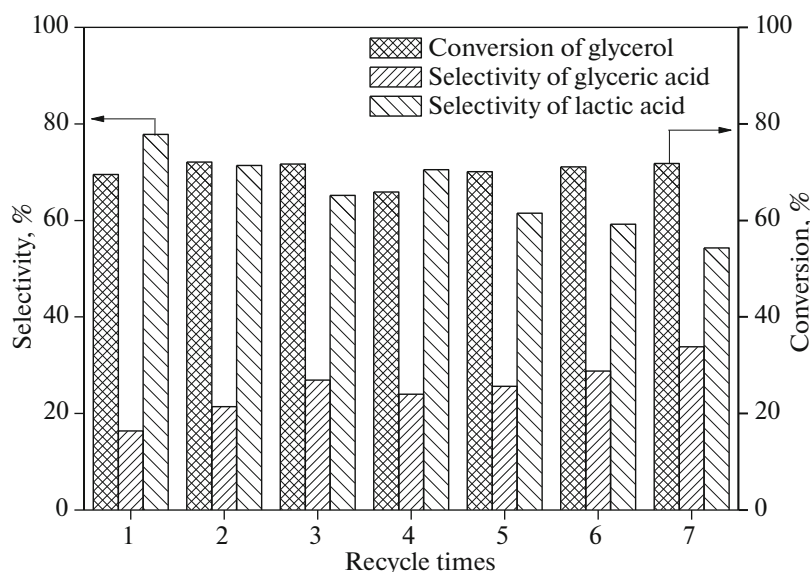


Fig. 8. The recycle times on catalyst performance for the Au–Pt/MgLaO catalyst.

dation activity and product distribution of glycerol. In addition, it was found that the catalytic activity of Au–Pt/MgLaO was better than that of monometallic Au and Pt catalysts, but the selectivity of lactic acid was slightly lower than that of the Pt/MgLaO catalyst.

Then, the Au–Pt/MgLaO catalyst was taken as the primary catalyst to study the effects of reaction conditions (e.g., reaction time, initial oxygen partial pressure, molar ratio of NaOH to glycerol, initial glycerol concentration) on the catalytic oxidation of glycerol and the selectivity for lactic acid. The results of experimental studies of glycerol oxidation on the Au–Pt/MgLaO catalyst under different conditions are listed in Table 4. The conversion of glycerol grew with the increase in reaction time (Table 4, entries 1–3). The conversion of glycerol increased from 69.0 to 86.2%, and the selectivity for lactic acid did not reveal a significant change. Similarly, the conversion of glycerol gradually grew with the increase in initial oxygen partial pressure (Table 4, entries 2, 4, and 5). However, the selectivity for lactic acid decreased with the increase in initial oxygen partial pressure, which indicated that higher oxygen pressure could inhibit further oxidation of glyceric acid to lactic acid, but increased the conversion of glycerol. When the molar ratio of NaOH to glycerol increased from 1 to 4 mol/mol (Table 4, entries 2 and 6), the conversion of glycerol increased from 83.1 to 92.9%, and the selectivity for lactic acid from 70.9 to 76.3%, which indicated that high concentration of NaOH promoted the formation of lactic acid. In addition, the effect of the initial glycerol concentration on the reaction was also investigated (Table 4, entries 2, 7–9). The conversion of glycerol decreased sharply with the increase in initial glycerol concentration, but the selectivity for lactic acid increased.

To evaluate the stability of the catalyst, the Au–Pt/MgLaO catalyst was tested for 7 runs, and the results are shown in Fig. 8. It can be seen that the catalyst has good catalytic activity and stability. After 7 cycles, the conversion of glycerol was ~70%, basically the same as in the first run. However, the selectivity towards lactic acid decreased from 77.8% in the first run to 54.3% in the seventh run. This can be explained by agglomeration of Au–Pt alloy particles during the reaction, which is evident from TEM micrographs of the catalysts before and after the first cycle (Figs. 2d, 3d).

### 3. CONCLUSIONS

In this study, a series of bimetallic Au–M (Pt, Pd, Cu, Ir, Ag) catalysts supported on composite oxide were prepared by the deposition of pre-formed Au–M colloids, and their catalytic performance was evaluated in selective oxidation of glycerol to lactic acid in alkaline conditions. Firstly, the support effect on catalytic performance was not significant in the selective oxidation of glycerol to lactic acid under alkaline condition. Secondly, the effect of the second active component of bimetallic Au–M catalysts supported on MgLaO composite oxide was investigated. The Au–Pt/MgLaO catalyst showed the best catalytic activity and the selectivity for lactic acid, followed by Au–Pd/MgLaO > Au–Cu/MgLaO > Au–Ir/MgLaO > Au–Ag/MgLaO. The synergistic effect of Au–M played a key role in the catalytic activity and product distribution in glycerol oxidation. Thirdly, the reaction conditions affect the catalytic activity and the selectivity for lactic acid. In addition, the Au–Pt/MgLaO catalyst also showed good cycle performance. After 7 cycles, the catalytic activity was not changed significantly, but the product selectivity decreased.

## ACKNOWLEDGMENTS

This work was supported by the Key Scientific Research Projects in 2017 at North Minzu University (grant no. 2017KJ15).

## REFERENCES

1. M. R. Monteiro, C. L. Kugelmeier, R. S. Pinheiro, M. O. Batalha, and A. D. César, *Renewable Sustainable Energy Rev.* **88**, 109 (2018).
2. G. Dodekatos, S. Schünemann, and H. Tüysüz, *ACS Catal.* **8**, 6301 (2018).
3. S. Li, W. P. Deng, Y. Y. Li, Q. H. Zhang, and Y. Wang, *J. Energ. Chem.* **32**, 138 (2019).
4. M. Dusselier, P. V. Wouwe, A. Dewaele, E. Makshina, and B. F. Sels, *Energy Environ. Sci.* **6**, 1415 (2013).
5. R. M. West, M. S. Holm, S. Saravanamurugan, J. M. Xiong, Z. Beversdorf, E. Taarning, and C. H. Christensen, *J. Catal.* **269**, 122 (2010).
6. P. Maki-Arvela, I. L. Simakova, T. Salmi, and D. Y. Murzin, *Chem. Rev.* **114**, 1909 (2014).
7. R. Palacio, S. Torres, D. Lopez, and D. Hernandez, *Catal. Today* **302**, 196 (2018).
8. W. P. Deng, Y. Z. Wang, S. Zhang, K. M. Gupta, M. J. Hulsey, H. Asakura, L. M. Liu, Y. Han, E. M. Karp, G. T. Beckham, P. J. Dyson, J. W. Jiang, T. Tanaka, Y. Wang, and N. Yan, *Proc. Natl. Acad. Sci. U. S. A.* **115**, 5093 (2018).
9. G. Y. Zhang, X. Jin, Y. A. Guan, B. Yin, X. B. Chen, Y. B. Liu, X. Feng, H. H. Shan, and C. H. Yang, *Ind. Eng. Chem. Res.* **58**, 14548 (2019).
10. S. M. A. H. Siddiki, A. S. Touchy, K. Kon, T. Toyao, and K. Shimizu, *ChemCatChem.* **9**, 2816 (2017).
11. Z. Y. Lu, I. Demianets, R. Hamze, N. J. Terrile, and T. J. Williams, *ACS Catal.* **6**, 2014 (2016).
12. G. Y. Yang, Y. H. Ke, H. F. Ren, C. L. Liu, R. Z. Yang, and W. S. Dong, *Chem. Eng. J.* **283**, 759 (2016).
13. W. Oberhauser, C. Evangelisti, C. Tiozzo, F. Vizza, and R. Psaro, *ACS Catal.* **6**, 1671 (2016).
14. M. Checa, F. Auneau, J. Hidalgo-Carrillo, A. Marinas, J. M. Marinas, C. Pinel, and F. J. Urbano, *Catal. Today* **196**, 91 (2012).
15. R. K. P. Purushothaman, J. van Haveren, I. Melian-Cabrera, E. R. H. van Eck, and H. J. Heeres, *ChemSusChem.* **7**, 1140 (2014).
16. C. Zhang, T. Wang, X. Liu, and Y. J. Ding, *Chin. J. Catal.* **37**, 502 (2016).
17. J. Ftouni, N. Villandier, F. Auneau, M. Besson, L. Djakovitch, and C. Pinel, *Catal. Today* **257**, 267 (2015).
18. S. E. Davis, M. S. Ide, and R. J. Davis, *Green Chem.* **15**, 17 (2013).
19. Y. H. Shen, S. H. Zhang, H. J. Li, Y. Ren, and H. C. Liu, *Chem-Eur. J.* **16**, 7368 (2010).
20. J. L. Xu, H. Y. Zhang, Y. F. Zhao, B. Yu, S. Chen, Y. B. Li, L. D. Hao, and Z. M. Liu, *Green Chem.* **15**, 1520 (2013).
21. R. K. P. Purushothaman, J. van Haveren, D. S. van Es, I. Melián-Cabrera, J. D. Meeldijk, and H. J. Heeres, *Appl. Catal. B* **147**, 92 (2014).
22. R. K. P. Purushothaman, J. van Haveren, A. Mayoral, I. Melian-Cabrera, and H. J. Heeres, *Top. Catal.* **57**, 1445 (2014).
23. C. Zhang, T. Wang, X. Liu, and Y. J. Ding, *J. Mol. Catal. A* **424**, 91 (2016).
24. Y. B. Li, S. Chen, J. L. Xu, H. Y. Zhang, Y. F. Zhao, Y. B. Wang, and Z. M. Liu, *Clea-Soil Air Water.* **42**, 1140 (2014).
25. H. J. Cho, C. C. Chang, and W. Fan, *Green Chem.* **16**, 3428 (2014).
26. S. C. Y. Tsen, P. A. Crozier, and J. Liu, *Ultramicroscopy* **98**, 63 (2003).
27. J. Dou, B. W. Zhang, H. Liu, J. D. Hong, S. M. Yin, Y. Z. Huang, and R. Xua, *Appl. Catal. B* **180**, 78 (2016).
28. D. Wang, A. Villa, F. Porta, D. S. Su, and L. Prati, *Chem. Commun.* **18**, 1956 (2006).
29. K. M. Pan, H. Ming, H. Yu, H. Huang, Y. Liu, and Z. H. Kang, *Dalton Trans.* **41**, 2564 (2012).
30. H. S. Oh, H. N. Nong, T. Reier, M. Gliech, and P. Strasser, *Chem. Sci.* **6**, 3321 (2015).
31. F. L. Zhang, Y. H. Zheng, Y. N. Cao, C. Q. Chen, Y. Y. Zhan, X. Y. Lin, Q. Zheng, K. M. Wei, and J. F. Zhu, *J. Mater. Chem.* **19**, 2771 (2009).
32. C. X. Qi, Y. H. Zheng, H. Lin, H. J. Su, X. Sun, and L. B. Sun, *Appl. Catal. B* **253**, 160 (2019).
33. B. E. Solsona, T. Garcia, C. Jones, S. H. Taylor, A. F. Carley, and G. J. Hutchings, *Appl. Catal. A* **312**, 67 (2006).
34. M. Saito, M. Itoha, J. Iwamoto, C. Y. Lia, and K. Machida, *Catal. Lett.* **106**, 107 (2006).
35. J. Gao, J. Z. Guo, D. Liang, Z. Y. Hou, J. H. Fei, and X. M. Zheng, *Int. J. Hydrogen Energy* **33**, 5493 (2008).
36. D. L. Wang, S. F. Lu, and S. P. Jiang, *Electrochim. Acta* **55**, 2964 (2010).
37. F. Şen and G. Gökağaç, *J. Phys. Chem. C* **111**, 5715 (2007).
38. J. F. Moulder, W. F. Stickle, P. E. Sobol, and K. D. Bomben, *Handbook of X-ray Photoelectron Spectroscopy* (Phys. Electron. Inc., Minnesota, 1995).
39. M. Brun, A. Berthet, and J. C. Bertolini, *J. Electron Spectrosc.* **104**, 55 (1999).
40. H. Meng, F. Y. Xie, J. Chen, and P. K. Shen, *J. Mater. Chem.* **21**, 11352 (2011).
41. A. A. Tapia, R. Zanella, C. Calers, C. Louis, and L. Delannoy, *Phys. Chem. Chem. Phys.* **17**, 28022 (2015).
42. L. C. Wang, Y. Zhong, H. J. Jin, D. Widmann, J. Weissmüller, and R. J. Behm, *Beilstein J. Nanotechnol.* **4**, 111 (2013).
43. Q. Q. Jia, D. F. Zhao, B. Tang, N. Zhao, H. D. Li, Y. H. Sang, N. Bao, X. M. Zhang, X. H. Xu, and H. Liu, *J. Mater. Chem. A* **38**, 16292 (2014).